ELSEVIER

Engineering Structures 24 (2002) 163–177

ENGINEERING STRUCTURES

www.elsevier.com/locate/engstruct

Non-linear analysis of shells of revolution with ring elements

Christian Lang [a,*], Rüdiger Meiswinkel [a], Filip C. Filippou [b]

[a] *Institute of Statics, University of Kaiserslautern, Erwin-Schrödinger-Straße, D-67663 Kaiserslautern, Germany*
[b] *Department of Civil and Environmental Engineering, University of California, Berkeley, CA 94720-1710, USA*

Received 2 May 2001; received in revised form 3 September 2001; accepted 6 September 2001

Abstract

This paper presents a ring element for the static analysis of shells of revolution of arbitrary shape under arbitrarily distributed loads, based on a displacement formulation that includes geometric and physical non-linearity. The trial functions for the displacement field in the circumferential direction of the shell involve harmonic series, so that the dependence in the circumferential direction is removed from the formulation. For this element, the derivation of the internal resisting force vector and of the tangent stiffness matrix is presented. Furthermore, the concept of ring elements is extended to a spring ring element for modelling uplift between a shell of revolution and the supporting ground. After the presentation of element theory, the use of these ring elements is demonstrated with two application studies.

Keywords: Shells of revolution; Shell ring elements; Physical and geometric non-linearity; Natural draught cooling towers

1. Introduction

Shells of revolution are used in a wide variety of engineering applications such as tanks, pressure vessels, digestion tanks or natural draught cooling towers. For the linear static and dynamic determination of the state of stress in these shells by the finite element method, ring elements are often employed. The basic idea of a ring element is to introduce Fourier series as trial functions for the unknown displacements in the circumferential direction of the shell. Thus, only the meridional direction has to be subdivided in separate elements, whereas one single ring element is used in circumferential direction.

Early research on ring elements dates back to the 1960s. Before that, numerical solution of the governing equations of shells of revolution was obtained by finite difference methods. Popov et al. [1] proposed a very simple conical ring element with constant wall thickness in 1964. Only axisymmetric problems were considered and, for this special case, the relationships between end forces of the ring element and nodal displacements were established. These end forces, of course, had a constant distribution in the circumferential direction on account of axisymmetry. The idea of ring elements has been extended by several researchers over the years: arbitrary wall thickness distribution and arbitrary curvature of the element's shape in the meridional direction were taken into account, as was the description of loads and displacements with the help of Fourier series in the circumferential direction, so that the limitation to axisymmetric problems was removed. In his book from 1985, which can be regarded as the state-of-the-art reference at the time, Gould [2] summarised the development for ring elements. As areas of application, the linear static and dynamic analysis of shells of revolution under arbitrary loads, the non-linear static analysis of shells of revolution under axisymmetric loads and the eigenvalue determination for frequencies and buckling loads under axisymmetric loads are described.

For modelling the non-linear behaviour of reinforced concrete shells, Grote [3] and Zahlten [4] introduced layer models into existing three-node and four-node elements formulated in curved coordinates. The deployment of ring elements for the task was not considered, even though their advantages were well known for the linear case. A reason for the reluctance of using ring elements under non-linear material behaviour might have been the loss of material uniformity in the circum-

* Corresponding author. Tel.: +49-631-205-2931; fax: +49-631-205-3901.
E-mail address: chrlang@rhrk.uni-kl.de (C. Lang).

0141-0296/02/$ - see front matter
PII: S0141-0296(01)00090-6

Nomenclature

A area of shell in undeformed configuration
$\mathbf{a}_1$, $\mathbf{a}_2$ covariant local basis vectors of middle surface of shell
$\mathbf{a}^1$, $\mathbf{a}^2$ contravariant local basis vectors of middle surface of shell; $\mathbf{a}^{\alpha}=a^{\alpha\lambda}\cdot\mathbf{a}_{\lambda}$
$\mathbf{a}_3$, $\mathbf{a}^3$ local basis vector perpendicular to shell middle surface
$a_{\alpha\beta}$ covariant components of metric tensor of shell middle surface
$a^{\alpha\beta}$ contravariant components of metric tensor of shell middle surface; $a^{\alpha\alpha}=1/a_{\alpha\alpha}$, $a^{12}=a^{21}=0$
a determinant of covariant components of metric tensor; $a=a_{11}a_{22}$
a_{gr} horizontal ground acceleration
$b_{\alpha\beta}$ covariant components of curvature tensor of shell middle surface
b^{α}_{β} mixed variant components of curvature tensor of shell middle surface; $b^{\alpha}_{\beta}=a^{\alpha\lambda}b_{\lambda\beta}$
c stiffness of supporting ground
E Young's modulus
$\mathbf{e}_1$, $\mathbf{e}_2$, $\mathbf{e}_3$ global Cartesian basis vectors
$\mathbf{G}$ transformation from physical element DOFs to multipliers of trial functions

$$\left[\begin{array}{cccccccc|cccc}
\sqrt{a_{11}^{A}} & 0 & 0 & 0 & 0 & 0 & 0 & 0 & 0 & 0 & 0 & 0\\
-\sqrt{a_{11}^{A}} & 0 & 0 & 0 & \sqrt{a_{11}^{B}} & 0 & 0 & 0 & -1 & -1 & 0 & 0\\
0 & \sqrt{a_{22}^{A}} & 0 & 0 & 0 & 0 & 0 & 0 & 0 & 0 & 0 & 0\\
0 & -\sqrt{a_{22}^{A}} & 0 & 0 & 0 & \sqrt{a_{22}^{B}} & 0 & 0 & 0 & 0 & -1 & -1\\
0 & 0 & 1 & 0 & 0 & 0 & 0 & 0 & 0 & 0 & 0 & 0\\
0 & -\Delta z b_2^{2A}\sqrt{a_{22}^{A}} & 0 & -\Delta z\sqrt{a_{22}^{A}} & 0 & 0 & 0 & 0 & 0 & 0 & 0 & 0\\
0 & 2\Delta z b_2^{2A}\sqrt{a_{22}^{A}} & -3 & 2\Delta z\sqrt{a_{22}^{A}} & 0 & \Delta z b_2^{2B}\sqrt{a_{22}^{B}} & 3 & \Delta z\sqrt{a_{22}^{B}} & 0 & 0 & 0 & 0\\
0 & -\Delta z b_2^{2A}\sqrt{a_{22}^{A}} & 2 & -\Delta z\sqrt{a_{22}^{A}} & 0 & -\Delta z b_2^{2B}\sqrt{a_{22}^{B}} & -2 & -\Delta z\sqrt{a_{22}^{B}} & 0 & 0 & 0 & 0\\
\hline
0 & 0 & 0 & 0 & 0 & 0 & 0 & 0 & 1 & 0 & 0 & 0\\
0 & 0 & 0 & 0 & 0 & 0 & 0 & 0 & 0 & 1 & 0 & 0\\
0 & 0 & 0 & 0 & 0 & 0 & 0 & 0 & 0 & 0 & 1 & 0\\
0 & 0 & 0 & 0 & 0 & 0 & 0 & 0 & 0 & 0 & 0 & 1
\end{array}\right]$$

g acceleration due to gravity (10 m/s^2)
H total shell height
h shell thickness
i, j counters for ring element DOFs; $1\le i, j\le 12$
k counter for integration points in meridional direction; $1\le k\le k_{max}$
$\mathbf{K}_{eu}$ global elastic stiffness matrix with initial displacement effects
$\mathbf{K}_{g}$ global geometric stiffness matrix
${}^{nm}k_{e}^{ji}$ term of linear elastic element stiffness matrix $\mathbf{k}_e$
${}^{nm}k_{eu}^{ji}$ term of elastic element stiffness matrix $\mathbf{k}_{eu}$ with initial displacements
${}^{nm}k_{g}^{ji}$ term of geometric element stiffness matrix $\mathbf{k}_g$
${}^{nm}k_{t}^{ji}$ term of tangent element stiffness matrix $\mathbf{k}_t$
l counter for integration points around half the circumference; $1\le l\le l_{max}$
l_{max} maximum number of integration points in circumferential direction for half the circumference (has to be an odd number, in this study $l_{max}=37$)
n, m counter for Fourier terms (number of waves in circumferential direction)
n_{max} maximum number of Fourier terms
$m^{\alpha\beta}$ components of bending moment tensor
$n^{\alpha\beta}$ components of membrane stress tensor
$\tilde{n}^{\alpha\beta}$ components of symmetric membrane stress tensor

$\mathbf{P}_e$ applied nodal force vector in global coordinates
$\mathbf{P}_i$ resisting force vector in global coordinates
$\mathbf{p}$ body force vector of shell; $\mathbf{p}=p^{\alpha}\cdot\mathbf{a}_{\alpha}+p^{3}\cdot\mathbf{a}_{3}$
${}^{n}p_e^{j}$ term of element force vector due to body forces
${}^{n}p_i^{j}$ term of element resisting force vector
R radius of meridian curve
$\mathbf{r}$ position vector to middle surface of shell
$\mathbf{u}$ displacement vector of shell middle surface; $\mathbf{u}=u_{\alpha}\cdot\mathbf{a}^{\alpha}+u_{3}\cdot\mathbf{a}^{3}$
$\mathbf{v}$ vector of element DOFs
${}^{k}W$ weight factors for Gauss integration in interval $0\leq\bar{z}\leq1$
${}^{l}W$ weight factors for Simpson integration;
${}^{l}W=4$ for even l, ${}^{l}W=2$ for odd l, ${}^{l}W=1$ for $l=1$ and $l=l_{\max}$ (first and last l)
δW_e virtual external work
δW_i virtual internal work
$\mathbf{w}$ displacement vector of shell normal vector; $\mathbf{w}=w_{\alpha}\cdot\mathbf{a}^{\alpha}$
x^1, x^2, x^3 coordinates in global system $\mathbf{e}_1$, $\mathbf{e}_2$, $\mathbf{e}_3$
$\bar{z}$ normalised element coordinate for meridional direction; $0\leq\bar{z}\leq1$
$\alpha_{\alpha\beta}$ components of strain tensor of middle surface relative to undeformed configuration (change of metric components $a_{\alpha\beta}$ due to deformation)
$\beta_{\alpha\beta}$ components of second strain tensor of middle surface relative to undeformed configuration (change of curvature components $b_{\alpha\beta}$ due to deformation)
$\Gamma^{\gamma}_{\alpha\beta}$ Christoffel symbols for middle surface of shell
δ^{β}_{α} Kronecker delta; 1 for $\alpha=\beta$, otherwise 0
$\varepsilon_{\alpha\beta}$ components of strain tensor of arbitrary shell layer outside middle surface relative to undeformed configuration
θ^1, θ^2, θ^3 local coordinates of shell
$\Delta\theta^1$ distance of integration points in circumferential direction; $\Delta\theta^1=\pi/(l_{\max}-1)$
μ square root of metric determinant of arbitrary layer relative to middle surface; $\sqrt{(a^{*}_{11}a^{*}_{22})/(a_{11}a_{22})}$
ν Poisson's ratio
ρ specific mass density
$\sigma^{\alpha\beta}$ components of second Piola Kirchhoff stress tensor (for the theory in this paper, approximately equal to Cauchy stress)
$\mathbf{\Phi}$ array of trial functions
$\varphi_{\alpha\beta}$, $\varphi_{\alpha3}$ displacement gradients for $\mathbf{u}$
$\bar{\varphi}_{\alpha\beta}$, $\bar{\varphi}_{\alpha3}$ displacement gradients for $\bar{\mathbf{u}}$
$\overset{+}{\varphi}_{\alpha\beta}$, $\overset{+}{\varphi}_{\alpha3}$ displacement gradients for $\overset{+}{\mathbf{u}}$
$\psi_{\alpha\beta}$, $\psi_{\alpha3}$ displacement gradients for $\mathbf{w}$
$\bar{\psi}_{\alpha\beta}$, $\bar{\psi}_{\alpha3}$ displacement gradients for $\bar{\mathbf{w}}$
$\overset{+}{\psi}_{\alpha\beta}$, $\overset{+}{\psi}_{\alpha3}$ displacement gradients for $\overset{+}{\mathbf{w}}$
$(\,)_{,\beta}$ partial differentiation with respect to β
$(\,)|_{\beta}$ covariant differentiation with respect to β: $u_{\alpha}|_{\beta}=u_{\alpha,\beta}-\Gamma^{\lambda}_{\alpha\beta}u_{\lambda}$; $u^{\alpha}|_{\beta}=u^{\alpha}{}_{,\beta}+\Gamma^{\alpha}_{\beta\lambda}u^{\lambda}$
$(\,)^{*}$ refers to arbitrary layer of shell outside the middle surface
${}^{n}(\,)$, ${}^{m}(\,)$ Fourier term n or m of an expression
$(\,)^{A}$, $(\,)^{B}$ expression evaluated at element node A or B
$\langle\ldots\rangle$ physical components

$\delta(\ldots)$	variation (independent variables are displacement increments $\overset{+}{\mathbf{u}}$)
$\overline{(\ldots)}$	dependence of term on known part of displacements $\overline{\mathbf{u}}$
$\overset{+}{(\ldots)}$	linear dependence of term on unknown displacement increments $\overset{+}{\mathbf{u}}$
$\overset{++}{(\ldots)}$	quadratic dependence of term on unknown displacement increments $\overset{+}{\mathbf{u}}$
${}^{k}(\ldots)$	expression at Gauss integration point k (meridional direction)
${}^{l}(\ldots)$	expression at Simpson integration point l (circumferential direction)

ferential direction under non-axisymmetric loads, even though Wunderlich and Rensch [5] developed ring elements for J2 plasticity models in steel applications. In 1994 Ravichandran et al. [6] proposed ring elements with geometric non-linearity. For material non-linearity, however, Gould [7] proposed a local–global concept in which the shell structure is divided into several parts: a portion that remains linear and is modelled by ring elements and a portion that is represented by isoparametric shell elements by discretisation in the meridional and circumferential direction. A suitable transformation for the common degrees of freedom (DOFs) of ring and isoparametric elements is used for coupling the two portions of the structure.

Baillis et al. [8] use ring elements for non-linear calculations of shells of revolution, originally based on a formulation by Combescure [9], taking into account arbitrarily distributed loads around the circumference and the non-linear material behaviour of reinforced concrete. These elements make use of linear interpolation functions in the meridional direction for all displacement components and the corresponding integration uses just one integration point. Eckstein et al. [10], on the other hand, propose cubic interpolation polynomials for all three components of the displacement vector. According to their examinations, linear displacement interpolation led to inaccurate results, especially for the first Fourier term n=1. Furthermore, problems at shell locations where bending moments arise might occur. These problems are solved by the use of cubic interpolation polynomials.

The objectives of this paper are to extend the ring element by Eckstein et al. [10] to account for general non-linear material response in the circumferential direction, to study the numerical behaviour of this type of shell element, and to verify its validity by correlation with available results from two application studies.

In the following, the element matrices for the non-linear element will be derived systematically. Then, the proposed concept will be transferred to the formulation of an uplift ring element. The validity of the proposed element for non-linear studies of shells of revolution will be demonstrated with two examples. The first example discusses the stress redistribution due to uplift from the foundation in a cylindrical shell under horizontal ground acceleration. The second example illustrates the stress redistribution due to cracking in a natural draught cooling tower under wind loading. In this example, the results obtained with the proposed ring elements are compared with results obtained with three-node and four-node shell elements in curved coordinates proposed by Grote [3]. In the following mathematical derivations, a tensor-based index notation is used following the book by Basar and Krätzig [11] with summation over repeated Greek indices. The proposed ring elements have been implemented in the finite element analysis program ROSHE [12].

2. Description of shell geometry

Fig. 1 shows the geometry of a ring element representing part of a shell of revolution. For the mathematical description of the middle surface, the equation of the meridian curve $R(\theta^2)$ and the wall thickness distribution $h(\theta^2)$ need to be specified. Furthermore, the local basis vectors $\mathbf{a}_\alpha$ of the middle surface in Fig. 1 are obtained by

$$\mathbf{a}_\alpha = \mathbf{r}_{,\alpha} \tag{1}$$

$$\text{with } \mathbf{r} = R(\theta^2)[\cos(\theta^1)\cdot\mathbf{e}_1 + \sin(\theta^1)\cdot\mathbf{e}_2] + \theta^2\cdot\mathbf{e}_3.$$

With the knowledge of basis vectors, the covariant components of the metric tensor, the covariant components of the curvature tensor and the Christoffel symbols can be established for this special type of geometry in the undeformed configuration as shown in Ref. [11].

These geometric variables depend on the meridian curve and its derivatives and can be determined at any point of the middle surface of the shell, so that no approximation of geometry is necessary. Furthermore, the ratio of the determinant of the metric components $a^*_{\alpha\beta}$ of a layer other than the middle surface and the determinant of the metric symbols $a_{\alpha\beta}$ at the middle surface is necessary for the stress integration through the depth:

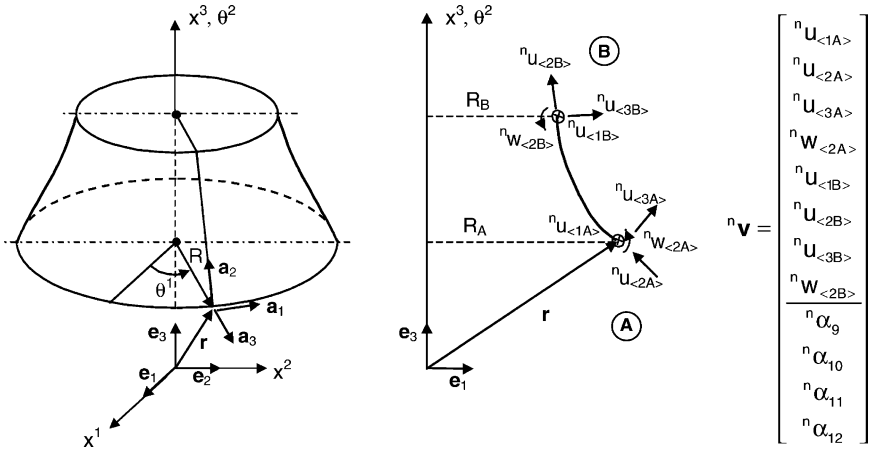

Fig. 1. Element geometry and degrees of freedom.

$$\mu(\theta^3)=\sqrt{\frac{a_{11}^{*}a_{22}^{*}}{a_{11}a_{22}}}=1-\theta^3\cdot[b_1^1+b_2^2]+(\theta^3)^2\cdot[b_1^1b_2^2]. \tag{2}$$

3. Approximation of displacement field

The three components of the displacement vector are expressed by Fourier series as shown in Eq. (3). This representation is based on the assumption of a plane of symmetry at $x^2=0$. If necessary, the corresponding antisymmetric parts can be easily included [8]; this, however, results in doubling the number of element DOFs. For most problems the assumption of symmetry is satisfactory:

$$\mathbf{u}(\theta^1,\theta^2)=\begin{bmatrix}u_1\\u_2\\u_3\end{bmatrix}=\sum_{n=0}^{n_{\max}}\begin{bmatrix}{}^{n}u_1(\theta^2)\sin(n\theta^1)\\{}^{n}u_2(\theta^2)\cos(n\theta^1)\\{}^{n}u_3(\theta^2)\cos(n\theta^1)\end{bmatrix}. \tag{3}$$

With Eq. (3), the description of the displacement distribution requires trial functions for the unknown Fourier coefficients ${}^{n}\mathbf{u}(\theta^2)$ in the meridional direction. Eckstein et al. [10] proposed cubic polynomials for these trial functions for each displacement component, because of their excellent performance in linear elastic analysis. In this case, the displacement field is represented by

$$\mathbf{u}(\theta^1,\theta^2)=\sum_{n=0}^{n_{\max}}{}^{n}\mathbf{\Phi}\cdot\mathbf{G}\cdot{}^{n}\mathbf{v}, \tag{4}$$

where

$${}^{n}\mathbf{\Phi}=\begin{bmatrix}s&\bar{z}s&0&0&0&0&0&0&\bar{z}^2s&\bar{z}^3s&0&0\\0&0&c&\bar{z}c&0&0&0&0&0&0&\bar{z}^2c&\bar{z}^3c\\0&0&0&0&c&\bar{z}c&\bar{z}^2c&\bar{z}^3c&0&0&0&0\end{bmatrix} \tag{5}$$

with

$$\bar{z}=\frac{\theta^2-\theta^{2A}}{\Delta z}\ \text{and}\ 0\le\bar{z}\le1\quad\text{(generalised coordinate)}$$

$$s=\sin(n\theta^1),\ c=\cos(n\theta^1),\ \Delta z=\theta^{2B}-\theta^{2A},$$

is the matrix of trial functions, and $\mathbf{G}$ provides the transformation from the actual element DOFs to the factors multiplying the trial functions in Eq. (5). The product of ${}^{n}\mathbf{\Phi}$ and $\mathbf{G}$ can be regarded as the displacement interpolation matrix for a single Fourier term.

The element DOFs are also shown in Fig. 1. They are defined for each term n of the Fourier series. Twelve element DOFs are necessary for the three cubic interpolation polynomials for each Fourier term. The proposed element has only eight physical DOFs (three displacements and one rotation at each node), so that four additional DOFs are introduced without physical relevance. Those can be either condensed out or assembled into free spaces of the global matrices where they do not interact with other DOFs. It is obvious from the last four rows and columns of matrix $\mathbf{G}$ that these DOFs are not subject to transformation.

4. Deformation and shell kinematics

In Fig. 2, the state of deformation of the shell is expressed by the displacement vector of the middle surface $\mathbf{u}$ and the difference $\mathbf{w}$ of the vector normal to the

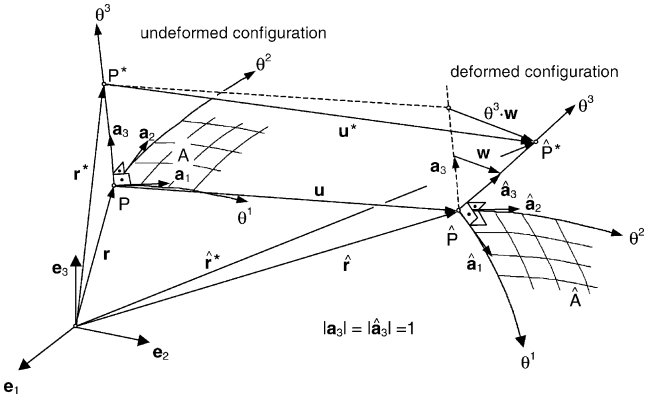

Fig. 2. Shell displacements.

middle surface before and after deformation. The displacement vector $\mathbf{u}^*$ of arbitrary point P* can thus be decomposed into

$$\mathbf{u}^*=\mathbf{u}+\theta^3\cdot\mathbf{w}. \tag{6}$$

For the theory of small rotations under the Kirchhoff–Love restriction of neglecting shear deformations in the proposed element, vector $\mathbf{w}$ is given by

$$w_\alpha=-[u_{3,\alpha}+u_\lambda b_\alpha^\lambda] \text{ and } w_3=0. \tag{7}$$

As shown by Basar and Krätzig [11], the strains of any shell layer are given by

$$\varepsilon_{\alpha\beta}(\theta^3)=\alpha_{\alpha\beta}+\theta^3\beta_{\alpha\beta}, \tag{8}$$

where higher-order terms in θ^3 are neglected. $\alpha_{\alpha\beta}$ [Eq. (9)] is the first strain tensor describing the change of metric of the middle surface due to deformation and $\beta_{\alpha\beta}$ [Eq. (10)] is the second strain tensor measuring the change of curvature, both relative to the original configuration:

$$\alpha_{\alpha\beta}=\frac{1}{2}[\varphi_{\alpha\beta}+\varphi_{\beta\alpha}+a^{\lambda\rho}\varphi_{\rho\alpha}\varphi_{\lambda\beta}+\varphi_{\alpha3}\varphi_{\beta3}] \tag{9}$$

with $\varphi_{\alpha\beta}=u_\alpha|_\beta-u_3 b_{\alpha\beta}$ and $\varphi_{\alpha3}=u_{3,\alpha}+u_\lambda b_\alpha^\lambda$,

$$\beta_{\alpha\beta}=\frac{1}{2}[\psi_{\alpha\beta}+\psi_{\beta\alpha}-\varphi_{\alpha\lambda}b_\beta^\lambda-\varphi_{\beta\lambda}b_\alpha^\lambda] \tag{10}$$

with $\psi_{\alpha\beta}=w_\alpha|_\beta$.

With these kinematic relations, only the first strain tensor $\alpha_{\alpha\beta}$ [Eq. (9)] is non-linear, whereas the second strain tensor $\beta_{\alpha\beta}$ [Eq. (10)] is linear in the deformations. This is known as the "theory of small rotations" (or Donnel–Marguerre-type theory with further simplifications in the non-linear contributions of the first strain tensor $\alpha_{\alpha\beta}$) and is satisfactory for most applications in civil engineering. A summary of different levels of shell theories (from the theory of large rotations to Donnel–Marguerre-type assumptions) can be found in Ref. [3].

5. Definition of stresses and material laws

The internal forces are derived from stress resultants, which are depicted in the positive direction in Fig. 3. The integration of stresses through the shell thickness yields the tensor of membrane forces $n^{\alpha\beta}$ [Eq. (11)], which is not symmetric, and the tensor of bending moments $m^{\alpha\beta}$ [Eq. (12)], in which higher-order terms in θ^3 are neglected. With the knowledge of metric symbols, calculation of physical stress components is possible as shown in Fig. 3:

$$n^{\alpha\beta}=\int_{-h/2}^{+h/2}\mu(\theta^3)[\delta_\lambda^\beta-\theta^3 b_\lambda^\beta]\sigma^{\alpha\lambda}(\theta^3)\,\mathrm{d}\theta^3=\tilde{n}^{\alpha\beta}-m^{\alpha\lambda}b_\lambda^\beta, \tag{11}$$

$$m^{\alpha\beta}=\int_{-h/2}^{+h/2}\mu(\theta^3)\theta^3\sigma^{\alpha\beta}(\theta^3)\,\mathrm{d}\theta^3. \tag{12}$$

Tensor $\tilde{n}^{\alpha\beta}$ in Eq. (11) is symmetric and energy conjugate to the first strain tensor of the middle surface [Eq. (9)], without having physical significance. For linear elastic, isotropic material response, Eqs. (13a) and (13b) relate stresses and strains:

$$\tilde{n}^{\alpha\beta}=\frac{Eh}{1-\nu^2}\cdot\frac{1-\nu}{2}[a^{\alpha\lambda}a^{\beta\rho}+a^{\alpha\rho}a^{\beta\lambda}+\frac{2\nu}{1-\nu}a^{\alpha\beta}a^{\lambda\rho}]\alpha_{\lambda\rho} \tag{13a}$$

and

$$m^{\alpha\beta}=\frac{Eh^3}{12[1-\nu^2]}\cdot\frac{1-\nu}{2}[a^{\alpha\lambda}a^{\beta\rho}+a^{\alpha\rho}a^{\beta\lambda}+\frac{2\nu}{1-\nu}a^{\alpha\beta}a^{\lambda\rho}]\beta_{\lambda\rho}. \tag{13b}$$

However, any plane stress material law can be used in Eqs. (11) and (12) with numerical integration over the shell thickness. A reinforced concrete model based on the paper by Cedolin and Mulas [13] for the non-linear elastic concrete behaviour in compression with enhance-

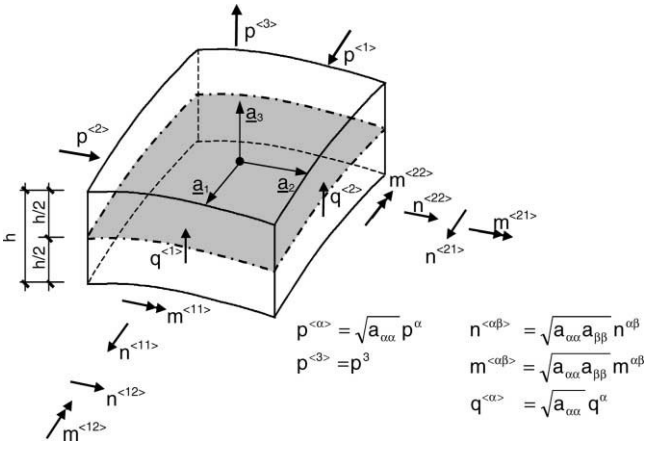

Fig. 3. Body forces and stress resultants of shell.

ments by Grote [3] and Meiswinkel [14], as implemented in ROSHE [12] and ROSHE3 [15], is used in the second application study of this paper. The effect of tension stiffening is accounted for by orthotropic relations. Shear forces are not significant in the present study, because shear deformations are neglected; if these are of interest, they can be determined from equilibrium.

6. Incremental formulation of principle of virtual displacements

Equilibrium in its weak form is formulated by the principle of virtual displacements: the structure's state of stress is in equilibrium if, under an arbitrary but admissible variation of displacements, the total virtual work is zero. In setting up the equation, the unknown displacements $\mathbf{u}$ are decomposed into a known part $\bar{\mathbf{u}}$ and an unknown increment $\overset{+}{\mathbf{u}}$, so that all variations of terms depending only on $\bar{\mathbf{u}}$ vanish:

$$u_i=\bar{u}_i+\overset{+}{u}_i \text{ and } \delta u_i=\delta\overset{+}{u}_i. \tag{14}$$

A similar decomposition is introduced for the first strain tensor and its variations,

$$\alpha_{\alpha\beta}=\bar{\alpha}_{\alpha\beta}+\overset{+}{\alpha}_{\alpha\beta}+\overset{++}{\alpha}_{\alpha\beta} \text{ and } \delta\alpha_{\alpha\beta}=\delta\overset{+}{\alpha}_{\alpha\beta}+\delta\overset{++}{\alpha}_{\alpha\beta}, \tag{15}$$

and the second strain tensor and its variations,

$$\beta_{\alpha\beta}=\bar{\beta}_{\alpha\beta}+\overset{+}{\beta}_{\alpha\beta} \text{ and } \delta\beta_{\alpha\beta}=\delta\overset{+}{\beta}_{\alpha\beta}. \tag{16}$$

Following Eqs. (17) and (18), the stress increments are established by computing the partial derivative of stresses with respect to strains, evaluated at the known state of strain. This is performed numerically by determining the material tangent operator in each layer, multiplying it with the corresponding strain increments in the layer, and integrating the resulting stress increments over the shell thickness:

$$\tilde{n}^{\alpha\beta}(\alpha_{\lambda\rho},\beta_{\lambda\rho})\approx\tilde{n}^{\alpha\beta}(\bar{\alpha}_{\lambda\rho},\bar{\beta}_{\lambda\rho})+\frac{\partial\tilde{n}^{\alpha\beta}}{\partial\alpha_{\lambda\rho}}(\bar{\alpha}_{\lambda\rho},\bar{\beta}_{\lambda\rho})\overset{+}{\alpha}_{\lambda\rho}+\frac{\partial\tilde{n}^{\alpha\beta}}{\partial\beta_{\lambda\rho}}(\bar{\alpha}_{\lambda\rho},\bar{\beta}_{\lambda\rho})\overset{+}{\beta}_{\lambda\rho}=\bar{\tilde{n}}^{\alpha\beta}+\overset{+}{\tilde{n}}^{\alpha\beta}, \tag{17}$$

$$m^{\alpha\beta}(\alpha_{\lambda\rho},\beta_{\lambda\rho})\approx m^{\alpha\beta}(\bar{\alpha}_{\lambda\rho},\bar{\beta}_{\lambda\rho})+\frac{\partial m^{\alpha\beta}}{\partial\alpha_{\lambda\rho}}(\bar{\alpha}_{\lambda\rho},\bar{\beta}_{\lambda\rho})\overset{+}{\alpha}_{\lambda\rho}+\frac{\partial m^{\alpha\beta}}{\partial\beta_{\lambda\rho}}(\bar{\alpha}_{\lambda\rho},\bar{\beta}_{\lambda\rho})\overset{+}{\beta}_{\lambda\rho}=\bar{m}^{\alpha\beta}+\overset{+}{m}^{\alpha\beta}. \tag{18}$$

The principle of virtual work with the inclusion of distributed loads acting only in and normal to the middle surface, as shown in Fig. 3,

$$\delta W_i+\delta W_e=0 \tag{19}$$

$$=-\int_A[\tilde{n}^{\alpha\beta}\delta\alpha_{\alpha\beta}+m^{\alpha\beta}\delta\beta_{\alpha\beta}]\,dA+\int_A[p^\alpha\delta u_\alpha+p^3\delta u_3]\,dA$$

leads to

$$\int_A[\overset{+}{\tilde{n}}^{\alpha\beta}\delta\overset{+}{\alpha}_{\alpha\beta}+\overset{+}{m}^{\alpha\beta}\delta\overset{+}{\beta}_{\alpha\beta}]\,dA+\int_A\bar{\tilde{n}}^{\alpha\beta}\delta\overset{++}{\alpha}_{\alpha\beta}\,dA$$

$$=\int_A[p^\alpha\delta\overset{+}{u}_\alpha+p^3\delta\overset{+}{u}_3]\,dA=\int_A\bar{\tilde{n}}^{\alpha\beta}\delta\overset{+}{\alpha}_{\alpha\beta}+\bar{m}^{\alpha\beta}\delta\overset{+}{\beta}_{\alpha\beta}]\,dA \tag{20}$$

where terms in the displacement increments with higher than quadratic order are neglected. After expressing the unknown increments in Eq. (20) in terms of node displacement increments, the global tangential stiffness relation yields

$$[\mathbf{K}_{eu}+\mathbf{K}_g]\cdot\overset{+}{\mathbf{V}}=\mathbf{P}_e-\mathbf{P}_i. \tag{21}$$

7. Derivation of element matrices

At this point, the increments of strain, stress and displacement in Eq. (20) need to be expressed in terms of the element DOFs with the help of the displacement interpolation functions (4). Numerical integration over the area of the ring element is necessary; Gauss integration with $k_{max}=3$ integration points is used in the meridional direction noting that the integration points and weights need to be transformed to the interval $0\le\bar{z}\le1$. Simpson integration is used in the circumferential direction in cases where the integral cannot be obtained in closed form. On account of symmetry, $l_{max}=37$ integration points over half the circumference are used. Consequently, the integrands in Eq. (20) need to be evaluated at $3\times37=111$ integration points.

7.1. Vector of applied forces

After expressing the displacement increments in terms of node displacements in the third term of Eq. (20), the force vector due to body forces is obtained by

$${}^np_e^j=\pi\Delta z\sum_k{}^kW\cdot{}^k(\sqrt{a})\cdot{}^k[{}^np^\alpha\cdot\overset{+}{u}_\alpha(\delta^n\overset{+}{v}{}^j) \tag{22}$$

$$+{}^{n}p^{3}\cdot\overset{+}{u}_{3}(\delta^{n}\overset{+}{v}^{j})]\cdot\begin{cases}2, & n=0\\ 1, & n\neq 0\end{cases},$$

where ${}^{n}p_{e}^{j}$ is the applied nodal force at element DOF j for Fourier term n. It is worth noting that integration is carried out in closed form in the circumferential direction, since the circumferential distribution of loads, which are expressed in Fourier series, and of the displacement increments is known in advance.

7.2. Vector of resisting forces

The fourth term in Eq. (20) yields the vector of resisting forces. The internal forces $\bar{\tilde{n}}^{\alpha\beta}$ and $\bar{m}^{\alpha\beta}$ due to the known strains $\bar{\alpha}_{\lambda\rho}$ and $\bar{\beta}_{\lambda\rho}$, as well as the variations of the strain increments due to node unit displacements $\delta^{n}\overset{+}{v}^{j}=1$, need to be determined at each integration point using the Simpson rule for numerical integration in the circumferential direction:

$${}^{n}p_{i}^{j}=\frac{2}{3}\Delta z\Delta\theta^{1}\sum_{k}{}^{k}W\cdot{}^{k}(\sqrt{a})\cdot\overset{k}{\left[\sum_{l}{}^{l}W\cdot{}^{l}[\bar{\tilde{n}}^{\alpha\beta}\cdot\overset{+}{\alpha}_{\alpha\beta}(\delta^{n}\overset{+}{v}^{j})\right.}\qquad(23)$$

$$\left.+\bar{m}^{\alpha\beta}\cdot\overset{+}{\beta}_{\alpha\beta}(\delta^{n}\overset{+}{v}^{j})]\right].$$

Again, ${}^{n}p_{i}^{j}$ denotes the internal force at element DOF j for Fourier term n.

7.3. Linear elastic stiffness matrix

The first term in Eq. (20) yields the elastic stiffness matrix. Assuming linear kinematic relations and linear elastic material response, the components of the linear elastic stiffness matrix can be set up as follows:

$${}^{nm}k_{e}^{ji}=\pi\Delta z\sum_{k}{}^{k}W\cdot{}^{k}(\sqrt{a})\cdot{}^{k}[\overset{+}{\tilde{n}}^{\alpha\beta}({}^{m}\overset{+}{v}^{i})\cdot\overset{+}{\alpha}_{\alpha\beta}(\delta^{n}\overset{+}{v}^{j})\qquad(24)$$

$$+\overset{+}{m}^{\alpha\beta}({}^{m}\overset{+}{v}^{i})\cdot\overset{+}{\beta}_{\alpha\beta}(\delta^{n}\overset{+}{v}^{j})]\cdot\begin{cases}2, & n=m=0\\ 1, & n=m\neq 0\\ 0, & n\neq m.\end{cases}$$

${}^{nm}k_{e}^{ji}$ is the nodal force increment at element DOF j of Fourier term n due to displacement increment at element DOF i of Fourier term m. The distribution of stress and strain increments in the circumferential direction is known in advance, since the relations are linear, and the corresponding integration can be carried out in closed form. An important property of the linear elastic stiffness matrix is that all terms except the main diagonal matrices ${}^{nn}k_{e}^{ji}$ are zero. Thus, the problem is uncoupled in the linear case: a node displacement increment in Fourier term m generates only nodal force increments for the same Fourier term; as consequence, the linear relation can be set up and solved independently for each Fourier term.

7.4. Tangent stiffness matrix

As shown in Eq. (20), the tangent stiffness matrix consists of two parts: the first part represents the elastic stiffness matrix, while the second part is the geometric stiffness matrix, which depends only on the known part of stress resultants $\bar{\tilde{n}}^{\alpha\beta}$ (bending moments $\bar{m}^{\alpha\beta}\bar{\tilde{n}}^{\alpha\beta}$ do not appear under the theory of small rotations) and on the variations of the quadratic increments of the first strain tensor. The components of the elastic stiffness [Eq. (25)] and the geometric stiffness matrix [Eq. (26)] are obtained by expressing the stress resultant increments and the variation of strain increments in the first two terms of Eq. (20) in terms of nodal unit displacements. The integration over the circumference is carried out numerically by the Simpson rule:

$${}^{nm}k_{eu}^{ji}=\frac{2}{3}\Delta z\Delta\theta^{1}\sum_{k}{}^{k}W\cdot{}^{k}(\sqrt{a})\cdot\qquad(25)$$

$$\overset{k}{\left[\sum_{l}{}^{l}W\cdot{}^{l}[\overset{+}{\tilde{n}}^{\alpha\beta}({}^{m}\overset{+}{v}^{i})\cdot\overset{+}{\alpha}_{\alpha\beta}(\delta^{n}\overset{+}{v}^{j})+\overset{+}{m}^{\alpha\beta}({}^{m}\overset{+}{v}^{i})\cdot\overset{+}{\beta}_{\alpha\beta}(\delta^{n}\overset{+}{v}^{j})]\right]},$$

$${}^{nm}k_{g}^{ji}=\frac{2}{3}\Delta z\Delta\theta^{1}\sum_{k}{}^{k}W\cdot{}^{k}(\sqrt{a})\cdot\qquad(26)$$

$$\overset{k}{\left[\sum_{l}{}^{l}W\cdot{}^{l}[\bar{\tilde{n}}^{\alpha\beta}\cdot\overset{++}{\alpha}_{\alpha\beta}(\delta^{n}\overset{+}{v}^{j},{}^{m}\overset{+}{v}^{i})]\right]},$$

with

$$\overset{++}{\alpha}_{\alpha\beta}(\delta^{n}\overset{+}{v}^{j},{}^{m}\overset{+}{v}^{i})=a^{\lambda\rho}\overset{+}{\varphi}_{\rho\alpha}(\delta^{n}\overset{+}{v}^{j})\cdot\overset{+}{\varphi}_{\lambda\beta}({}^{m}\overset{+}{v}^{i})\qquad(27)$$

$$+\overset{+}{\varphi}_{\alpha 3}(\delta^{n}\overset{+}{v}^{j})\cdot\overset{+}{\varphi}_{\beta 3}({}^{m}\overset{+}{v}^{i}).$$

The sum of elastic and geometric stiffness matrices represents the element tangent stiffness matrix,

$${}^{nm}k_{t}^{ji}={}^{nm}k_{eu}^{ji}+{}^{nm}k_{g}^{ji},\qquad(28)$$

where the indices have the same meaning as for the linear elastic stiffness matrix. It should be noted that, in general, the tangent stiffness matrix is fully occupied under non-linear response. Thus, a displacement increment in Fourier term m leads to nodal force increments in a different Fourier term n, in contrast to the linear case. Consequently, the tangent stiffness matrix is super-diagonal at the start of the analysis. The off-diagonal submatrices of the element stiffness matrix

appear with the onset of non-linear behaviour (e.g., non-symmetric stiffness distribution around the circumference due to cracking). In the application examples of this paper, a modified Newton algorithm is used for the solution of the global stiffness relation, so that it is not necessary to use the exact tangent stiffness matrix. Instead, the equilibrium iterations are carried out with a super-diagonal stiffness matrix that consists of submatrices ${}^{nn}k_t^{ji}$ [Eq. (28)], while off-diagonal matrices ($n \neq m$) are neglected. This approach maintains the decoupling of Fourier terms in the determination of displacement increments, but results in more iterations near the ultimate load of the structure when significant non-linear material response takes place.

A different approach for the solution of the non-linear equilibrium equations is the pseudo-load method as shown by Ravichandran et al. [6], where the error from neglecting the off-diagonal coupling stiffness terms is corrected at the element level. However, this method requires an additional iteration loop for each load increment and subsequent equilibrium iteration.

8. Spring ring element for uplift from foundation

The proposed ring element concept can be readily extended to account for uplift of the shell support from the foundation. To this end, the derivation of a spring ring element is shown with only vertical displacements in the global x^3 direction. The spring ring element has only one DOF ${}^n v$ for each Fourier term n, so that numbering of element DOFs is not necessary. The vector of resisting forces [Eq. (30)] and the tangent stiffness matrix [Eq. (31)] can be set up with the same trial functions for vertical displacements in the global direction by taking account of symmetry:

$$u_{\langle 2\rangle} = \sum_{n=0}^{n_{\max}} {}^n v \cos(n\theta^1), \tag{29}$$

$${}^n p_i = \frac{2}{3}\Delta\theta^1 R \sum_l {}^l W \cdot {}^l [c \cdot \bar{u}_{\langle 2\rangle} \cdot \overset{+}{u}_{\langle 2\rangle} (\delta^n \overset{+}{v})] \tag{30}$$

and

$${}^{nm}k_t = \frac{2}{3}\Delta\theta^1 R \sum_l {}^l W \cdot {}^l [c \cdot \overset{+}{u}_{\langle 2\rangle} ({}^m \overset{+}{v}_{\langle 2\rangle}) \cdot \overset{+}{u}_{\langle 2\rangle} (\delta^n \overset{+}{v}_{\langle 2\rangle})]. \tag{31}$$

Here, c is the stiffness of the ground at each integration point in the circumferential direction; this term is set to zero when uplift ($\bar{u}_{\langle 2\rangle} > 0$) takes place.

9. Application studies

The following two application studies demonstrate the use of the proposed shell ring element and the spring ring element in non-linear static analysis. The first example deals with the static response of a cylindrical shell under horizontal earthquake excitation. The shell is allowed to uplift from the foundation. The second example shows the results of a non-linear stress analysis of a natural draught cooling tower under wind loading.

9.1. Cylindrical shell under dead load and horizontal ground acceleration

The first study deals with a cylindrical shell under dead load and horizontal ground acceleration. The description of the shell geometry requires the following parameters: radius R=5.0 m, total height H=20.0 m and wall thickness h=0.20 m. A linear elastic material is selected with Young's modulus E=3.0×10^7 kN/m^2 and Poisson's ratio ν=0.20. At the shell base, the displacements u_1 tangential to the circumference and u_3 normal to the shell middle surface are suppressed. In the global vertical direction the shell is supported by an elastic foundation that allows uplift with stiffness

$$c(\theta^1) = \begin{cases} 10^5 \text{ kN/m}^2, & \text{no uplift} \\ 0, & \text{uplift.} \end{cases} \tag{32}$$

The specific weight for the shell material is equal to ρ=2.5 t/m^3 and the imposed ground acceleration has peak value a_{gr}=4.0 m/s^2. With these values, the load components can be expressed in a Fourier series by

$$p^{\langle 1\rangle} = -\rho a_{gr} h \sin(\theta^1) = -2.5\times 4.0\times 0.2 \sin(\theta^1) = -2.0 \text{ kN/m}^2 \sin(\theta^1), \tag{33a}$$

$$p^{\langle 2\rangle} = -\rho g h = -2.5\times 10.0\times 0.2 = -5.0 \text{ kN/m}^2 \tag{33b}$$

and

$$p^{\langle 3\rangle} = +\rho a_{gr} h \cos(\theta^1) = +2.5\times 4.0\times 0.2 \cos(\theta^1) = +2.0 \text{ kN/m}^2 \cos(\theta^1). \tag{33c}$$

It is readily seen that the dead load [Eq. (33b)] only contributes to Fourier term n=0, whereas the horizontal ground acceleration contributes to Fourier term n=1. The only non-linear response in this example derives exclusively from the uplift at the base of the shell, while the shell kinematics and material response have been assumed to remain linear. All pertinent structural and material data are summarised in Fig. 4, where the finite element model is also shown.

In the following, the results for membrane force $n^{\langle 22\rangle}$ and ring bending moment $m^{\langle 11\rangle}$ are discussed. In the linear case with no uplift, a closed-form solution for the meridional force $n^{\langle 22\rangle}$ can be established from the statically determinate membrane solution, which yields

$$n^{\langle 22\rangle} = -5.0\times[20-\theta^2] - 0.4\times[20-\theta^2]^2 \cos(\theta^1) \text{ kN/m}. \tag{34}$$

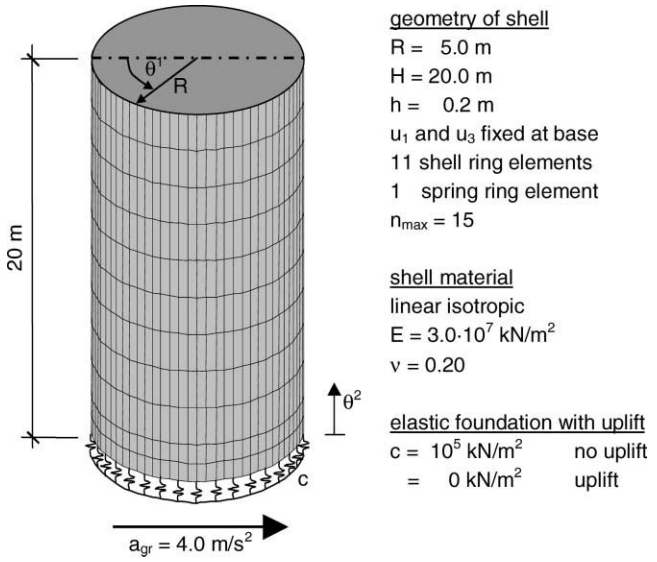

Fig. 4. Geometry and properties of cylindrical shell.

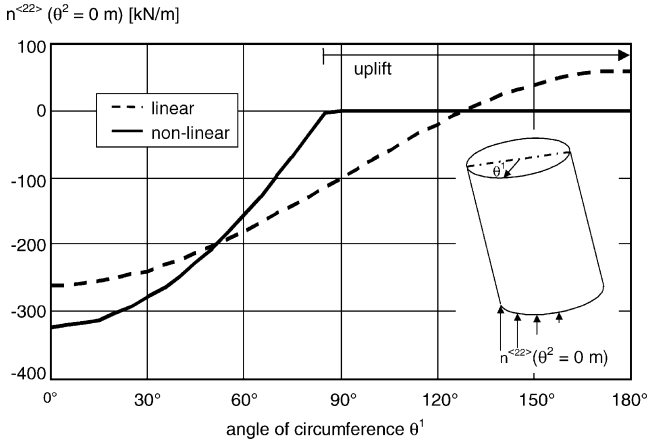

Fig. 5. Linear and non-linear supporting forces at the shell's base.

The bending moments are zero under pure membrane action. Obviously, only those Fourier terms n=0 and n=1 that appear in the expression for the loads [Eqs. (33)] appear in the linear solution for the meridional force $n^{\langle 22\rangle}$ and all other pertinent forces. The minimum and maximum meridional forces arise at the shell base. These are $n^{\langle 22\rangle}(\theta^1=0°, \theta^2=0\text{ m})=-260$ kN/m and $n^{\langle 22\rangle}(\theta^1=180°, \theta^2=0\text{ m})=60$ kN/m. For this load combination, the shell will uplift from the ground because tensile meridional forces cannot be transferred to the

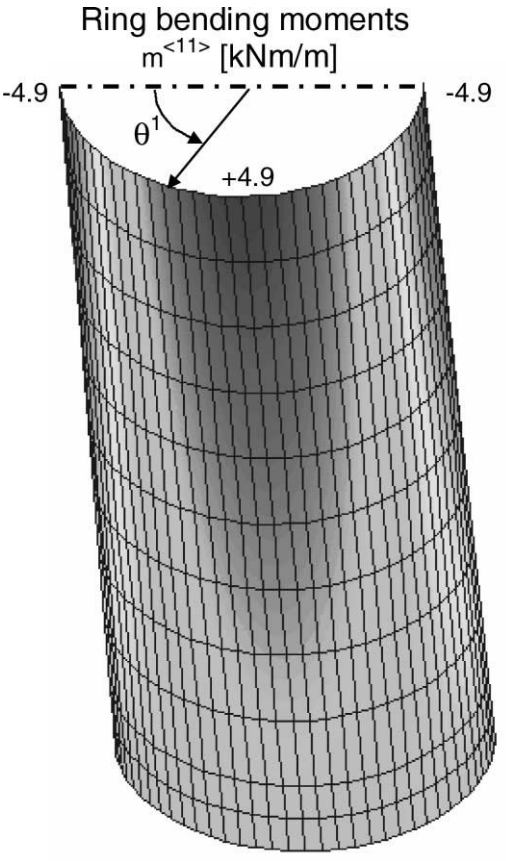

Fig. 6. Ring bending moments $m^{\langle 11\rangle}$ caused by uplift.

ground. The non-linear meridional stress distribution around the circumference at the base under uplift is depicted in Fig. 5 and the numerical values are summarised in Table 1. It is obvious that uplift increases the largest compressive force at θ^1=0° from −260 kN/m to −323 kN/m. The region under uplift extends from θ^1=90° to θ^1=270° on account of symmetry. It can be readily confirmed that the non-linear stress distribution for $n^{\langle 22\rangle}$ satisfies equilibrium with the total vertical force of 3141.6 kN due to dead load and the total moment of 12,566.5 kNm relative to the shell base due to horizontal ground acceleration. The allowance for uplift also gives rise to shell bending moments $m^{\langle 11\rangle}$ in contrast to the linear solution of pure membrane action. Fig. 6 shows the distribution of circumferential bending moments $m^{\langle 11\rangle}$ due to uplift. The circular shape of the circumference is not maintained in the upper regions of the shell

Table 1
Non-linear distribution of meridional forces $n^{\langle 22\rangle}$ at the shell's base

θ^1	0°	5°	10°	15°	20°	25°	30°	35°	40°
$n^{\langle 22\rangle}$ (kN/m)	−322.9	−321.7	−318.0	−311.9	−303.5	−292.6	−279.5	−264.1	−246.4
θ^1	45°	50°	55°	60°	65°	70°	75°	80°	85°
$n^{\langle 22\rangle}$ (kN/m)	−226.7	−204.8	−181.1	−155.4	−128.1	−99.1	−68.7	−36.9	−3.9

and it deforms to an oval, giving rise to circumferential bending moments. The maximum value of these moments takes place at the top end of the shell and is equal to $m^{\langle 11\rangle}(\theta^2=20\text{ m})=-4.90\cos(2\theta^1)$ kNm/m. The moments are decreasing towards the base of the shell, since no distortion to an oval shape can take place there on account of the boundary conditions. These moments arise due to external forces in Fourier terms n=0 (dead load) and n=1 (horizontal ground acceleration), generating contributions in higher Fourier terms. Naturally, all resisting force terms ${}^n p_i^j$ vanish for $n>1$ after the iterative solution algorithm has converged; in this state, the applied forces and the internal resisting forces are in equilibrium. Nonetheless, Fourier terms with $n>1$ have to be carried through the entire iteration process since out-of-balance forces in these terms lead to displacement increments for $n>1$. The number of Fourier terms to carry in the equilibrium iterations is a matter of judgement and in this study the trial functions have Fourier terms to n_{max}=15. However, for $n>6$, no effect on the results can be detected, so that the Fourier expansion of the solution could have been limited to a smaller number of terms. In this application, the Fourier term n=2 produces significant contributions to the non-linear solution and must not be neglected. Finally, the convergence behaviour is summarised in Table 2 for two different tolerances. Uplift starts at an acceleration of 2.5 m/s^2. Below this limit, all load steps converge in one iteration with a residual around 10^{-15}. Above this limit, due to non-linear behaviour, the number of iterations increases significantly. Depending on the tolerance for the out-of-balance forces, the last load step (4.0 m/s^2) requires 34 iterations (62 iterations for a higher tolerance) to converge.

9.2. Cooling tower shell under dead load and wind load

The second example refers to the shell of the "Boxberg" cooling tower in Germany. A simplified model of this cooling tower neglecting the influence of the supporting beam columns and the upper ring beam has been studied in a collapse analysis by Meiswinkel [14] under the load combination of 1.15DL+λWL (DL: dead load, WL: wind load). The analysis resulted in an ultimate load factor of λ=1.98 for the wind load [14].

Table 2
Convergence behaviour of cylindrical shell

a_{gr} (m/s^2)	Force tolerance	
	$\varepsilon=10^{-3}$	$\varepsilon=10^{-5}$
0.00	1 iteration	1 iteration
1.00	1 iteration	1 iteration
2.00	1 iteration	1 iteration
3.00	6 iterations	12 iterations
4.00	34 iterations	62 iterations

The meridian curve of the cooling tower below the throat is given by

$$R(\theta^2)=-15.3644+51.9644\sqrt{1+\left(\frac{\theta^2-115.83}{113.9896}\right)^2},\quad \theta^2\le 115.83\text{ m} \tag{35a}$$

and the curve above the throat by

$$R(\theta^2)=36.3422+0.2578\sqrt{1+\left(\frac{\theta^2-115.83}{8.0293}\right)^2},\quad \theta^2>115.83\text{ m}. \tag{35b}$$

In this study, the shell is modelled with ring elements and the non-linear stress distributions are compared with the results from an analysis using four-node and three-node shell elements in curved coordinates as implemented in ROSHE3 [15] [two-dimensional (2D) element mesh, 18 four-node and 36 three-node elements, respectively, around half the circumference]. For reinforced concrete, the plane stress isotropic non-linear elastic material law proposed by Cedolin and Mulas [13] for the biaxial compression region is used; a rotating crack model has been used in the tensile region and tension stiffening effects have been introduced as equivalent concrete stressess as described by Grote [3] and Meiswinkel [14]. Stresses are determined in each shell layer and then integrated through the depth to yield the internal force resultants. Fig. 7 shows the structural model with 23 ring elements. Material data and reinforcement amounts are provided in Fig. 8. The wind load is expanded into a Fourier series (n_{max}=15) and the same number of Fourier terms is selected for the representation of displacements in the circumferential direction.

In Fig. 9 the crack distribution on both sides of the shell surface is shown. An extended crack region around the meridian at $\theta^1=0°$ can be seen; these cracks which are caused by tensile meridional forces $n^{\langle 22\rangle}$ under wind loading extend through the whole shell thickness. Cracks also arise in the upper regions of the shell, but these are caused by ring bending moments $m^{\langle 11\rangle}$ and do not extend through the shell thickness. Thus, non-axisymmetric cracking gives rise to similar effects as those observed under uplift in the previous application. To explain this behaviour, Fig. 10 shows the distribution of meridional force $n^{\langle 22\rangle}$ at meridian $\theta^1=0°$ over the height of the shell under both linear and non-linear response. The model with ring elements and the model with 18 four-node shell elements around half the circumference yield essentially identical results. The maximum value of the linear elastic meridional force $n^{\langle 22\rangle}$=836 kN/m takes place at a height of θ^2=73.6 m. Where this force exceeds the tensile strength of the material, cracking takes place as is

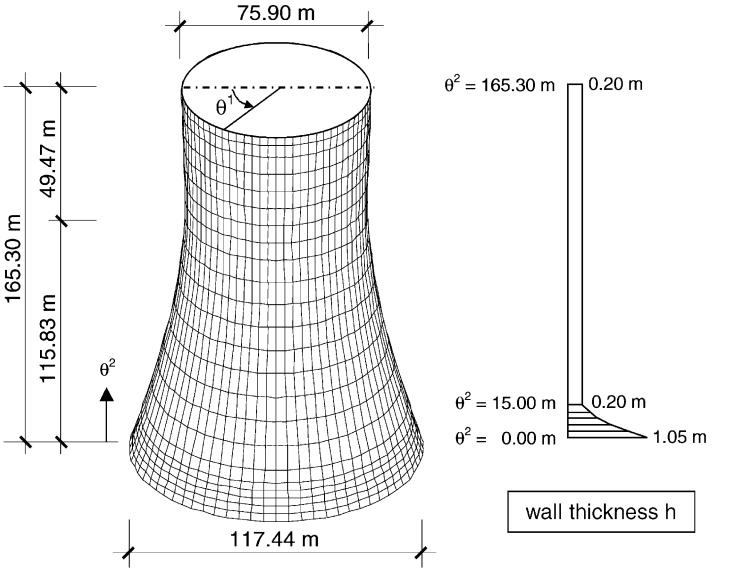

23 shell ring elements, n_{max} = 15 (description of wind load and displacements)

boundary conditions
top: free
bottom: hinged

loadings
dead load: $\gamma = 25.2$ kN/m³

wind load: $p^{<3>} = -0.9\cdot[[\theta^2+11.17]/10]^{0,22} \cdot 1.06 \cdot c_p(\theta^1)$

with $c_p(\theta^1) = 1 - 2 \cdot [\sin(90/70\cdot\theta^1)]^{2,267}$ 0° - 70°
$- 1 + 0.5 \cdot [\sin(90/21\cdot[\theta^1-70])]^{2,395}$ 70° - 91°
$- 0.5$ 91° -180°

combination: 1.15 DL + 1.75 WL

Fig. 7. Geometry and properties of finite element model for the "Boxberg" cooling tower.

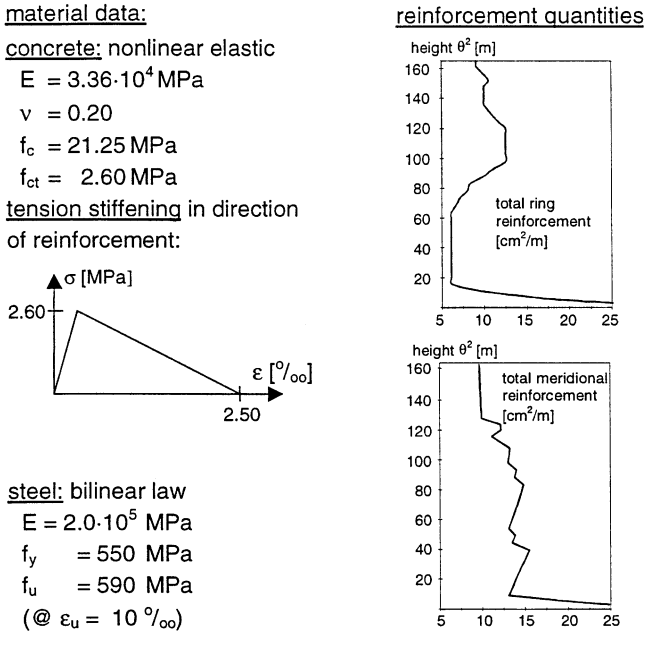

Fig. 8. Material data and reinforcement amounts for the "Boxberg" cooling tower

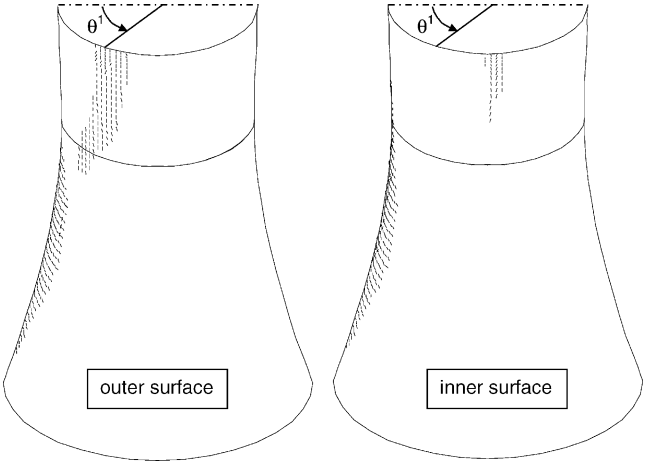

Fig. 9. Crack distributions due to 1.15DL+1.75WL.

evident in Fig. 9. As a result of cracking, the maximum meridional force $n^{\langle 22\rangle}$ reduces from 836 kN/m to 556 kN/m in this meridian. The distribution of meridional forces $n^{\langle 22\rangle}$ around the circumference at a height of θ^2=73.6 m is shown in Fig. 11. At the transition point between the cracked and uncracked regions at θ^1=25°, a sharp discontinuity is evident in the distribution. It should be noted that the cracking force of the cross-sec-

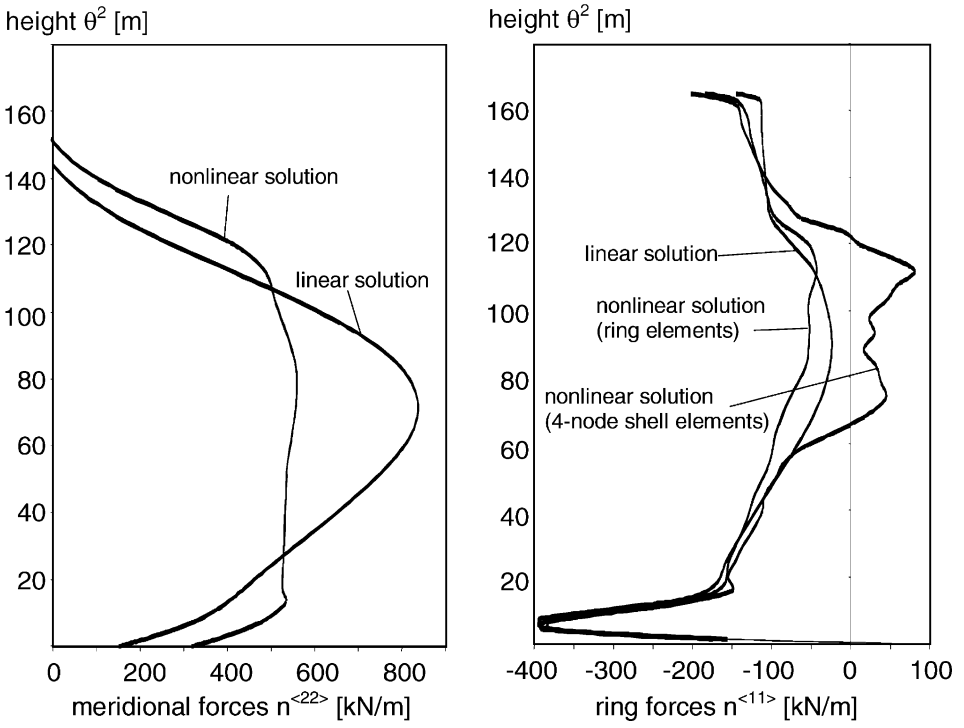

Fig. 10. Membrane forces in meridian θ^1=0°.

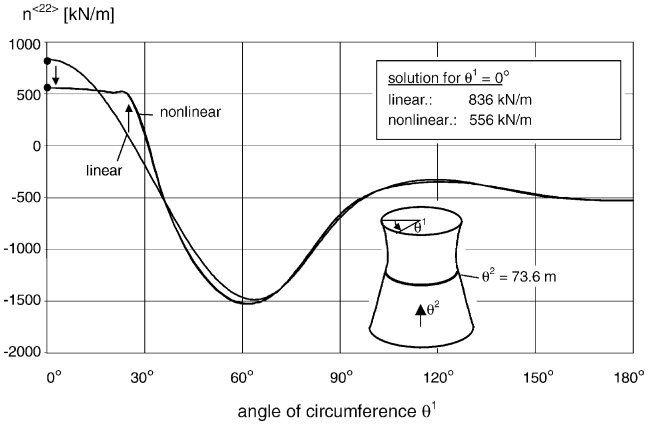

Fig. 11. Meridional forces $n^{\langle 22\rangle}$ at height θ^2=73.6 m.

tion at this height is $f_{ct}\cdot h$=520 kN/m when neglecting the reinforcement contribution. Approximately at θ^1=25°, this value is exceeded. Between θ^1=0° and θ^1=25°, a significant reduction of stiffness relative to the uncracked portion of the circumference takes place, so that tensile forces redistribute from the maximum at θ^1=0° to the uncracked region between θ^1=20° and θ^1=35°, as can be seen from the force distributions in Fig. 11. From θ^1=60° to θ^1=180°, no significant difference exists between the linear and the non-linear solution, since the whole backside of the shell remains uncracked.

Furthermore, the ring forces $n^{\langle 11\rangle}$ at the meridian θ^1=0° are also shown in Fig. 10. The linear solutions agree well for both ring elements and four-node shell elements. But the non-linear solutions at the meridian θ^1=0° show differences. In the model with four-node shell elements, tensile forces are computed between θ^2=70 m and θ^2=120 m. On the other hand, the non-linear solution with ring elements shows an increase of the compressive forces relative to the linear solution. For the height θ^2=73.6 m, where the maximum linear tensile meridional force $n^{\langle 22\rangle}$ takes place, the distribution of the corresponding ring forces $n^{\langle 11\rangle}$ around the circumference is shown in Fig. 12. Between θ^1=0° and θ^1=70°, the non-linear solution changes significantly relative to the linear solution. Furthermore, the non-linear solution with four-node shell elements oscillates around the non-linear solution with ring elements in this range of the circumfer-

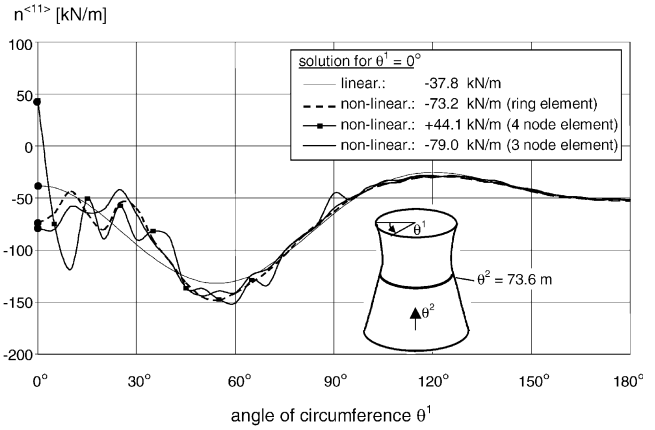

Fig. 12. Ring forces $n^{\langle 11\rangle}$ at height θ^2=73.6 m.

ence. The midpoint stresses of the four-node elements (marked with squares) show good agreement with the ring element solution, but the forces at the boundaries of the four-node elements do not agree. This discrepancy becomes especially obvious near the symmetry axis. Compared with the linear solution of $n^{\langle 11\rangle}(\theta^1=0°)=-37.8$ kN/m, the non-linear solution with ring elements increases to $n^{\langle 11\rangle}(\theta^1=0°)=-73.2$ kN/m and the non-linear solution with four-node quadrilateral elements changes to a tensile force of $n^{\langle 11\rangle}(\theta^1=0°)=+44.1$ kN/m. Membrane equilibrium shows that the reduction of meridional forces from $n^{\langle 22\rangle}(\theta^1=0°)=836$ kN/m to 556 kN/m caused by cracking requires an increase of the ring forces at the symmetry axis, as is the case for the non-linear solution with ring elements. Membrane equilibrium can be written as (e.g., Basar and Krätzig [11])

$$n^{\alpha\beta}b_{\alpha\beta}=-p^3\Leftrightarrow n^{\langle 11\rangle}=-p^{\langle 3\rangle}\frac{a_{11}}{b_{11}}-n^{\langle 22\rangle}\frac{b_{22}a_{11}}{b_{11}a_{22}}. \tag{36}$$

With the covariant components of the metric and curvature tensors from the equation of the meridian curve of the cooling tower [Eq. (35a)] (angle of 9° against the vertical axis) and with the loads normal to shell,

$$\begin{aligned} &p^{\langle 3\rangle}(\theta^1=0°,\ \theta^2=73.6\text{ m})=-1.15\times 25.2\text{ kN/m}^3\\ &\times 0.2\text{ m}\times\sin(9°)-1.75\times 1.06\times 0.90\text{ kN/m}^2\\ &\times\left(\frac{11.17+73.63}{10}\right)^{0.22}=-3.58\text{ kN/m}^2, \end{aligned} \tag{37}$$

the linear ring force $n^{\langle 11\rangle}(\theta^1=0°)$ corresponding to the linear meridional force of $n^{\langle 22\rangle}(\theta^1=0°)=836$ kN/m can be calculated by

$$n^{<11>}=3.58\times\frac{1603.7}{-39.554}-836\times\frac{0.0033\times 1603.7}{-39.554\times 1.025}= \tag{38}$$

$$-36.0\text{ kN/m}$$

and the non-linear ring force $n^{\langle 11\rangle}(\theta^1=0°)$ corresponding to the non-linear meridional force $n^{\langle 22\rangle}(\theta^1=0°)=556$ kN/m can be calculated by

$$n^{\langle 11\rangle}=3.58\times\frac{1603.7}{-39.554}-556\times\frac{0.0033\times 1603.7}{-39.554\times 1.025}= \tag{39}$$

$$-72.6\text{ kN/m}.$$

With these approximate calculations, the results of the ring element model at the axis of symmetry can be validated. Eq. (36) shows that the reduction of meridional forces $n^{\langle 22\rangle}(\theta^1=0°)$ caused by cracking results in an increase of absolute value of the corresponding compressive ring forces in order to maintain equilibrium. It should be noted that these approximate calculations are just used to validate the trend of the non-linear solution. It is not intended to create the impression that the four-node shell elements produce inaccurate results. First of all, no discrepancies are evident under linear elastic material response. Furthermore, the midpoint ring forces of the four-node element solution agree very well with the corresponding forces of the ring element solution. Thus, the only conclusion that can be derived from this example is that discrepancies may arise when stresses are calculated at the boundaries of four-node shell elements. A mesh refinement with 36 four-node elements (not shown in this paper) over half of the circumference that increases the numerical effort significantly shows much better accuracy in the $n^{\langle 11\rangle}$ distribution at the boundaries, and no oscillation takes place.

Furthermore, the results of a third approach are depicted in Fig. 12. Hereby, 36 three-node shell elements around half of the circumference (two three-node elements substituting one four-node element) have been used. Compared with the four-node shell elements, these three-node shell elements are formulated with a higher (fifth-order) displacement interpolation polynomial [15]. Even at the boundaries of the three-node shell elements, the non-linear ring forces improve significantly towards the ring element solution. But as drawbacks of this model, an increase in the total number of DOFs and in the total computational effort by setting up and solving the incremental stiffness relation has to be mentioned. In this application study, the advantage of ring elements for the strain and stress determination in the circumferential direction becomes obvious. Very satisfactory results are achieved, since the displacement field can be continuously differentiated around the circumference as often as desired. So with these higher-order three-node shell elements, the results of the proposed ring elements can be validated.

10. Conclusions

This paper presents the extension of the linear elastic shell ring element by Eckstein et al. [10] to account for non-linear kinematic relations and non-linear material response in shells of revolution. A theory of small rotations has been used neglecting all of the non-linear contributions in the second strain tensor, which is sufficient for most applications in civil engineering. A ring spring element that describes the uplift of the shell base from the foundation is also derived from the same idea. The main idea of these ring elements is to represent the displacement field in the circumferential direction by means of Fourier series. These ring elements have several advantages relative to commonly used shell elements: (1) no discretisation is necessary in the circumferential direction, (2) the accuracy of the results in this direction is controlled by the number of Fourier terms, (3) the displacement field can be continuously differentiated in the circumferential direction without reducing the order of the trial functions, thus leading to

better strain and stress approximation in this direction, and (4) the computational effort is reduced on account of the smaller number of global degrees of freedom. However, a major shortcoming of ring elements is the restriction to axisymmetric structures. For example, shells of revolution with cut-outs cannot be modelled with the proposed approach. In such a case, the local–global concept proposed by Gould can be used whereby general shell elements are used to represent geometric regions with cut-outs, while ring elements are deployed in the rest of the shell, including regions of non-linear material response. The number n_{max} of 15 Fourier terms used in the examples presented in this paper is an upper bound for cases of smooth external load distributions. In many cases a smaller number is sufficient and results in significant reductions of computational effort. Nonetheless, it is important to ensure that the selected order of the Fourier series is able to represent accurately the real displacement field (comparable with mesh refinements in 2D models). It is important to note that the stiffness matrix of the proposed ring elements is super-diagonal in the linear elastic case, since off-diagonal submatrices vanish on account of the orthogonality of Fourier terms. However, this desirable property is lost under non-linear response, which results in coupling of the different Fourier terms. To preserve this feature and reduce the computational effort, a modified Newton type solution strategy is proposed in this paper, with a super-diagonal stiffness matrix: the terms of the element stiffness matrix on the main diagonal are updated with the state, but the off-diagonal submatrices are neglected. The contribution of off-diagonal submatrices only becomes significant with extensive non-linear behaviour near the collapse load of the structure, resulting in a higher number of equilibrium iterations for these load steps.

For non-linear dynamic analysis the proposed algorithm is very attractive on account of the super-diagonal nature of the mass matrix, which dominates the effective stiffness matrix of the structure for small time steps. Thus, the proposed ring element can be used to great advantage for the seismic response analysis of shells of revolution, particularly since very few Fourier terms are necessary for the representation of the displacement field in this case.

The ring element concept can be extended to other types of structural members, as demonstrated in this paper for a ring spring element that represents the uplift of the shell base from the foundation. Another interesting example could be the development of a ring beam element for shell stiffeners. In conclusion, ring elements are an excellent choice for the linear and non-linear static and dynamic analysis of shells of revolution.

Acknowledgements

This study was conducted by the first author during his stay as a visiting scholar at the University of California at Berkeley from April 2000 to March 2001. This stay was supported by a scholarship from the German Academic Exchange Institution (DAAD) within a special college programme. This financial support is gratefully acknowledged.

References

[1] Popov EP, Penzien J, Lu Z-A. Finite element solution for axisymmetrical shells. J Eng Mech Div 1964;90(5):119–45.
[2] Gould PL. Finite element analysis of shells of revolution. Boston (MA): Pitman Advanced Publishing Program, 1985.
[3] Grote K. Theorie und Anwendung geometrisch und physikalisch nichtlinearer Algorithmen auf Flächentragwerke aus Stahlbeton. Report No. 1992/1. Kaiserslautern: Institute of Statics, University of Kaiserslautern, 1992.
[4] Zahlten W. A contribution to the physically and geometrically nonlinear computer analysis of general reinforced concrete shells. Report No. 90-2. Bochum: Institute of Statics and Dynamics, Ruhr-University of Bochum, 1990.
[5] Wunderlich W, Rensch HJ. A semi-analytical finite element process for nonlinear elastoplastic analysis of arbitrarily loaded shells of revolution. In: Transactions of the 6th International Conference on Structural Mechanics in Reactor Technology (SMiRT-6), Paris, 1981. Amsterdam: North-Holland, 1982, (paper M 4/1*).
[6] Ravichandran RV, Sridharan S, Gould PL. A local–global model for the non-linear analysis of locally defective shells of revolution. Int J Num Meth Eng 1994;37:3057–74.
[7] Gould PL. Local–global finite element analysis of shells of revolution. In: Wunderlich W, editor. European Conference on Computational Mechanics (ECCM 99), Munich, 1999.
[8] Baillis C, Jullien JF, Limam A, Chauvel D, Duval C. Study of the mechanical behaviour of a cooling tower subjected to the wind pressure with a 2D approach. In: Proceedings of SEWC 1998, San Francisco (CA), 1998. Amsterdam: Elsevier Science Ltd, 1998, (paper T157-5).
[9] Combescure A. Static and dynamic buckling of large thin shells. Nucl Eng Design 1986;92:339–54.
[10] Eckstein U, Krätzig WB, Wittek U. Finite-Element-Berechnungen zur Grenztragfähigkeit der Rotationsschalen. Report No. 80-4. Bochum: Institute of Statics and Dynamics, Ruhr-University of Bochum, 1980.
[11] Basar Y, Krätzig WB. Mechanik der Flächentragwerke. Braunschweig: Vieweg and Sohn, 1985.
[12] Wittek U, Meiswinkel R, Lang C. Manuals for the finite element program ROSHE. Kaiserslautern: Institute of Statics, University of Kaiserslautern, 1999.
[13] Cedolin L, Mulas MG. Biaxial stress–strain relation for concrete. J Eng Mech 1984;110(2):187–206.
[14] Meiswinkel R. Entwurf von Stahlbeton-Flächentragwerken unter Berücksichtigung wirklichkeitsnaher Strukturanalysen. Report No. 1998/1. Kaiserslautern: Institute of Statics, University of Kaiserslautern, 1998.
[15] Wittek U, Meiswinkel R. Manuals for the finite element program ROSHE3. Kaiserslautern: Institute of Statics, University of Kaiserslautern, 1999.